Chinese Journal of
POLYMER SCIENCE

RESEARCH ARTICLE

https://doi.org/10.1007/s10118-026-3763-x
Chinese J. Polym. Sci.

Hydrogen Bonding in Gel Polymer Electrolyte Enables High Performance High-mass-loading Silicon Anode

Xin-Ran Bi[a,b], Ze-Hui Fan[b], Lan-Hua Ma[b], and Yun-Hua Xu[a,b*]

[a] *School of Energy (National Industry-Education Platform for Energy Storage), Tianjin University, Tianjin 300072, China*
[b] *School of Materials Science and Engineering, State Key Laboratory of Advanced Materials for Intelligent Sensing, Tianjin University, Tianjin 300072, China*

Electronic Supplementary Information

Abstract Although silicon is a promising anode material for high-energy-density lithium-ion batteries, the huge volume change during the cycling leads to collapse of the electrode structure and fast degradation, particularly for the high-mass-loading electrodes. This has severely hindered its practical application. Here, a crosslinked polymer gel electrolyte is developed for high-mass-loading Si electrode. The gel electrolyte was fabricated by *in situ* polymerization method using methyl methacrylate and *N*,*N*′-methylenebisacrylamide as the monomer and crosslinking agent, respectively. It forms hydrogen bonds with hydroxyl groups on the surface of silicon anode to fix silicon particles and shows high oxidative stability to be compatible with high voltage cathode. With such gel polymer electrolyte, a high-mass-loading Si anode at 3.5 mg·cm^{-2} achieves a largely improved cycling stability, with a high reversible capacity of 1462.4 mAh·g^{-1}. Furthermore, full cells using the high-mass-loading Si anode and $LiNi_{0.8}Co_{0.1}Mn_{0.1}O_2$ cathode demonstrate exceptional cycling performance with a high capacity retention of 75.8% after 1000 cycles at 1 C, and stable cycling even at a high temperature of 60 °C. Our findings provide an effective strategy to promote the practical application of high-mass-loading Si anode for high energy density lithium ion batteries.

Keywords Lithium-ion battery; High-mass-loading silicon anode; Gel polymer electrolyte; *In situ* polymerization; Hydrogen bonding

Citation: Bi, X. R.; Fan, Z. H.; Ma, L. H.; Xu, Y. H. Hydrogen bonding in gel polymer electrolyte enables high performance high-mass-loading silicon anode. *Chinese J. Polym. Sci.* https://doi.org/10.1007/s10118-026-3763-x

INTRODUCTION

Lithium-ion batteries (LIBs) have been widely used in consumer electronics, electric vehicles, and renewable energy storage systems. However, meeting the future demand for high-energy density and enhanced safety remains a significant challenge. Currently, LIBs rely on flammable organic liquid electrolytes and graphite anodes. Flammable electrolytes pose substantial safety risks, whereas the low specific capacity of graphite (372 mAh·g^{-1}) limits the overall energy density of LIBs.[1] Advanced electrodes and electrolyte materials are essential to meet the requirements of next-generation high-performance LIBs.[2–10]

Si possesses an exceptionally high theoretical capacity of approximately 4200 mAh·g^{-1} and abundant natural reservoirs,[4–7,11–19] making it one of the most promising alternatives to graphite anodes for high-energy-density LIBs. Despite these advantages, Si anodes face critical challenges that hinder their practical applications. Si undergoes enormous volume changes (>300%) during lithiation and delithiation processes, which can lead to severe particle pulverization, electrode delamination, and continuous rupture and reformation of the solid electrolyte interphase (SEI).[20–23] These structural and interfacial instabilities result in rapid capacity fading and low Coulombic efficiency, severely limiting the practical application of silicon anodes. Numerous strategies have been explored to mitigate these issues, including the design of Si/C composites,[24–26] nanostructured silicon materials,[27] and advanced binders.[28] However, many of these sophisticated material designs involve complex synthesis procedures that are challenging to scale up for practical applications.

In addition to electrode design, electrolyte engineering has emerged as an effective approach for stabilizing Si anodes.[29] Conventional flammable organic liquid electrolytes suffer from several inherent drawbacks, including leakage, fire or explosion risk, and poor ability to accommodate large volume changes of the silicon anode during cycling.[30–32] Recently, gel polymer electrolytes (GPEs) have been applied to silicon anodes, offering improved safety and electrochemical performance.[12,33,34] The polymer matrix provides enhanced mechanical strength to maintain the integrity of silicon particles and electrodes, while enhancing safety by immobilizing solvent molecules to prevent leakage. Various polymer matrices have been employed, but most of them exhibit weak bonding interactions with the silicon anode. This limits the Si anode at low mass loadings and leads to poor cycling performance, hindering their practical application in high-energy-

* Corresponding author, E-mail: yunhua.xu@tju.edu.cn
Received April 23, 2026; Accepted May 30, 2026; Published online August 19, 2026

density batteries. For example, Liu *et al.*[35] reported a GPE utilizing methylene bis(acrylamide) and silica-nanoresin in Si|NCM811 cells and obtained improved cycling performance, but the mass loading of the silicon anode was only 1 mg·cm^{-2}. Huang *et al.*[36] designed a GPE based on poly(poly(tetramethylenether) glycol-*co*-4,4′-methylene diphenyl diisocyanate)-ethylene diamine), and used it on a high-mass-loading silicon anode (3.0 mAh·cm^{-2}@4.7 mg·cm^{-2}), while the insufficient cycling performance was presented with 70.0% capacity retention after 350 cycles.

In this work, we report a crosslinked polymethyl methacrylate-based GPE (PMMA-GPE) fabricated *via* an *in situ* polymerization method for high-mass-loading silicon anodes, using methyl methacrylate (MMA) and *N*,*N*′-methylenebisacrylamide (MBA) as the monomer and crosslinking agent, respectively. The cross-linked polymer not only provides a robust matrix, but also forms hydrogen bonding interactions between the abundant carbonyl groups of the polymer matrix and the hydroxyl groups on the surface of the silicon anode, significantly enhancing its stability. For a high-mass-loading Si anode at 3.5 mg·cm^{-2}, a high reversible capacity of 1462.4 mAh·g^{-1} is obtained. When paired with a $LiNi_{0.8}Co_{0.1}Mn_{0.1}O_2$ (NCM811) cathode, the Si|NCM811 cells showed excellent stability, retaining 75.8% capacity retention after 1000 cycles at a high current density of 1 C and enhanced thermal stability even at 60 °C. This study provides an effective strategy for stabilizing high-mass-loading silicon anodes using a facile *in situ* polymerization method (Fig. 1), paving the way for high-energy-density and safe LIBs.

EXPERIMENTAL

Materials

Ehylene carbonate (EC), diethyl carbonate (DEC), ethyl methyl carbonate (EMC), ffuoroethylene carbonate (FEC), Lithium hexaffuorophosphate ($LiPF_6$), lithium diffuoro(oxalato) borate (LiDFOB) were purchased from Dodo Chem. Methyl methacrylate (MMA) was purchased from Shanghai Aladdin Biochemical Technology Co., Ltd. The Si anode (SiO_x, 3.5 mg·cm^{-2}) and NCM811 cathode (N/P=1.05) were kindly provided by the China Automotive Battery Research Institute Co., Ltd.

Battery Fabrication

A conventional liquid electrolyte (LE) composed of 1 mol·L^{-1} $LiPF_6$ and 0.2 mol·L^{-1} LiDFOB in ethylene carbonate (EC)/diethyl carbonate (DEC)/ethyl methyl carbonate (EMC) (1/1/1, *V*/*V*/*V*) with 10 wt% fluoroethylene carbonate (FEC) was prepared under argon atmosphere. To prepare the PMMA-GPE, methyl methacrylate (MMA, 10 wt%) and *N*,*N*′-methylenebisacrylamide (MBA, 1 wt%) were added to the liquid electrolyte and stirred for 0.5 h. Then, 2,2′-azobis(2-methylpropionitrile) (AIBN, 0.2 wt%) was added as initiator to prepare the precursor solution. After the battery was assembled, the precursor solution was polymerized at 60 °C for 5 h.

CR2032 coin-type Si|NCM811 and the corresponding half-cells were assembled using the electrolyte prepared above (40 μL) and polypropylene (PP, Celgard 2500) separators in an argon-filled glove box (O_2 and H_2O < 0.1×10^{-6}).

Electrochemical Measurements

Cycling performance and rate performance tests were conducted using a NEWARE CT4008T battery test system. The ionic conductivities of the electrolytes were measured by electrochemical impedance spectroscopy (EIS). The EIS test was performed in the frequency range of 10^{-2}–10^{6} Hz at a potentiostatic signal with an amplitude of 5 mV. The stainless-steel (SS)|electrolyte|SS cells were employed to obtain the bulk resistances of the various electrolytes. The corresponding σ value was calculated using the following equation:

$$\sigma = \frac{L}{R \times S} \tag{1}$$

where L represents the distance between two blocking electrodes, R is the measured bulk resistance, and S is the effective area of the electrolyte in contact with the SS electrodes. Electrochemical impedance spectroscopy (EIS) measurements and linear cyclic voltammetry (LSV) were performed on a Solartron 1470 electrochemical workstation. The LSV curves were examined from 0 V to 6 V at a scan rate of 0.1 mV·s^{-1}. The lithium-ion transference number (t_{Li^+}) was determined using Li symmetric cells *via* EIS and potentiostatic polarization tests. t_{Li^+} is calculated from the BruceVincent-Evans equation:

$$t_{Li^+} = \frac{I_{SS}}{I_0} \times \frac{\Delta V - I_0 \times R_0}{\Delta V - I_{ss} \times R_{ss}} \tag{2}$$

where I_{ss} and I_0 represent the steady-state and initial currents, respectively, R_0 and R_{ss} represent the interface resistance before and after polarization, respectively. ΔV is the applied polariza-

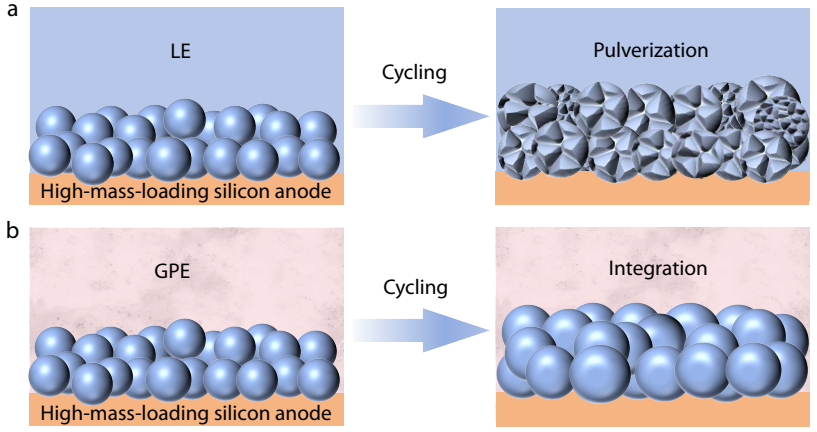

Fig. 1 Schematic illustration of a high-mass-loading silicon anode during cycling in (a) LE and (b) PMMA-GPE.

https://doi.org/10.1007/s10118-026-3763-x

tion voltage.[37]

For the galvanostatic intermittent titration technique (GITT) experiments, a current pulse of 0.1 A·g^{-1} was applied to the battery for 1200 s, and then the relaxation potential of the battery was measured for 3600 s without applying current. The GITT data were used to calculate the Li^+ diffusion coefficient (D_{Li^+}) at various voltages using the following equation:

$$D_{Li^+} = \frac{4}{\pi\tau}\left(\frac{m_B V_M}{M_B S}\right)^2\left(\frac{\Delta E_s}{\Delta E_t}\right)^2 \quad (3)$$

where m_B is the mass of the active substance on the electrode (g), M_B is the molar mass (g·mol^{-1}), V_M is the molar volume (cm^3·mol^{-1}), S is the area of the electrode plate (cm^2), τ is the relaxation time (s), ΔE_s is the steady-state potential change due to the current pulse, and ΔE_t is the potential change in the current pulse after subtracting the iR drop.[38]

Characterizations

Fourier transform infrared (FTIR) spectra were obtained using a Bruker Alpha spectrophotometer (placed in an argon-filled glove box) in the range 400–4000 cm^{-1}. The concentration of TMs dissolved in the electrolyte was obtained by inductively coupled plasma optical emission spectrometry (ICP-OES, Agilent 5800) with an RF power of 1.2 kW and a retrieval time of 5 s. The cycled cells were carefully disassembled in a glovebox and the cycled Si electrodes were washed with dimethyl carbonate (DMC, 99%, Aladdin) and dried at 25 °C. The morphologies of the Si anodes were examined by scanning electron microscopy (SEM) using a Hitachi Regulus 8100 instrument. X-ray photoelectron spectroscopy (XPS) measurements were carried out using a Thermo Fisher K-Alpha instrument with an Al K*α* source at an ion energy of 1000 eV. X-ray diffraction (XRD) patterns were obtained using a Rigaku Ultima IV diffractometer with Cu-Kα radiation (*λ*=1.5406 Å, 40 kV, 40 mA). The Bruker nuclear magnetic resonance (^{7}Li-NMR) spectra of the powders were recorded on a Bruker AVANCE NEO 800 MHz spectrometer using dimethyl sulfoxide-d_6 as the solvent. Thermogravimetric analysis (TG) was performed using a TG 209 F3 Tarsus analyzer under a N_2 atmosphere at a heating rate of 10 °C·min^{-1} from room temperature to 500 °C.

Simulation Details

The highest occupied molecular orbital (HOMO) and lowest unoccupied molecular orbital (LUMO) energy levels were determined using the Gaussian 09 W software. All calculations were performed using the B_3LYP functional.

RESULTS AND DISCUSSION

Fig. 2(a) shows the polymerization of MMA and MBA. Fourier transform infrared spectroscopy (FTIR) confirmed the successful formation of the polymer network (Fig. 2b). Specifically, the disappearance of the characteristic absorption peaks at approximately 1625 cm^{-1} (C=C) and 3065 cm^{-1} (=C—H) indicated the consumption of vinyl groups during polymerization. Meanwhile, the presence of characteristic functional groups at 1721 cm^{-1} (O—C=O) and 1540 cm^{-1} (NH—C=O) demonstrated the successful crosslinking between MMA and MBA, resulting in the formation of PMMA-GPE.

In addition to covalent chain formation during polymerization, MMA and MBA can also interact *via* hydrogen bonding. The carbonyl groups (—C=O) in MMA can form multiple hydrogen bonds with both the carbonyl (—C=O) and amine (N—H) groups of MBA, as well as with the polar hydroxyl groups (—OH) on the surface of the Si particles.[35,39] These interactions promote the formation of a robust cross-linked polymer network that effectively encapsulates silicon particles and reinforces the structural integrity of the electrode (Fig. 2c). As shown in Fig. S1 (in the electronic supplementary information, ESI), the FTIR spectra show the peak of the hydroxyl group at 3425 cm^{-1} for the silicon anode, which indicates a hydrogen bonding interaction between the polymer matrix and the silicon anode.

The structure of PMMA-GPE was further investigated by X-ray diffraction (XRD). The XRD pattern indicated that PMMA-GPE exhibited a typical amorphous structure, which facilitated lithium-ion migration (Fig. S2 in ESI). To further understand the electrochemical properties of the electrolyte components, density functional theory (DFT) calculations were performed. As shown in Fig. 2(d), MMA exhibits a higher highest occupied molecular orbital (HOMO) energy level (–7.61 eV) and a lower lowest unoccupied molecular orbital (LUMO) energy level (–1.53 eV) compared to other electrolyte components of ethylene carbonate (EC), diethyl carbonate (DEC), and ethyl methyl carbonate (EMC). This indicates that MMA is more likely to undergo oxidation and reduction reactions, thereby participating in the formation of the cathode electrolyte interphase (CEI) and solid electrolyte interphase (SEI). In addition, FEC and MBA exhibited lower LUMO energy levels, suggesting that they were preferentially reduced on the Si anode surface, which facilitated the formation of a stable SEI layer containing N-, F-, and B-based inorganic components.

The thermal stability of the polymer electrolyte was evaluated by thermogravimetric analysis (TG). As shown in Fig. S3 (in ESI), PMMA-GPE exhibited a significantly lower weight-loss rate than the conventional liquid electrolyte, indicating enhanced thermal stability. This improvement arises from the PMMA-based polymer network, which effectively immobilizes the liquid electrolyte components and suppresses their volatilization at elevated temperatures.

The electrochemical stability windows (ESW) of PMMA-GPE and LE were evaluated using linear sweep voltammetry (LSV) (Fig. 2e). The LE begins to undergo severe decomposition at approximately 4.5 V. In contrast, PMMA-GPE significantly expanded the ESW to approximately 5.5 V, indicating improved electrochemical stability. Furthermore, PMMA-GPE exhibits a high ionic conductivity (σ) of 0.73 mS·cm^{-1} at 25 °C, which is comparable to that of LE (1.01 mS·cm^{-1}) (Fig. 2f). According to the Bruce-Vincent-Evans equation, PMMA-GPE demonstrates a significantly higher lithium-ion transference number (t_{Li^+}) of 0.64 at 25 °C, in contrast 0.36 to LE (Fig. 2g and Fig. S4 in ESI). This improvement can be attributed to the formation of a cross-linked polymer network, which restricts anion mobility and promotes lithium-ion transport. The increased lithium-ion transference number effectively alleviated the concentration polarization within the battery, thereby maintaining a uniform Li^+ concentration at the electrode-electrolyte interface.

The solvation structure of the electrolyte was investigated by Raman spectroscopy. As shown in Fig. 2(h), the relative

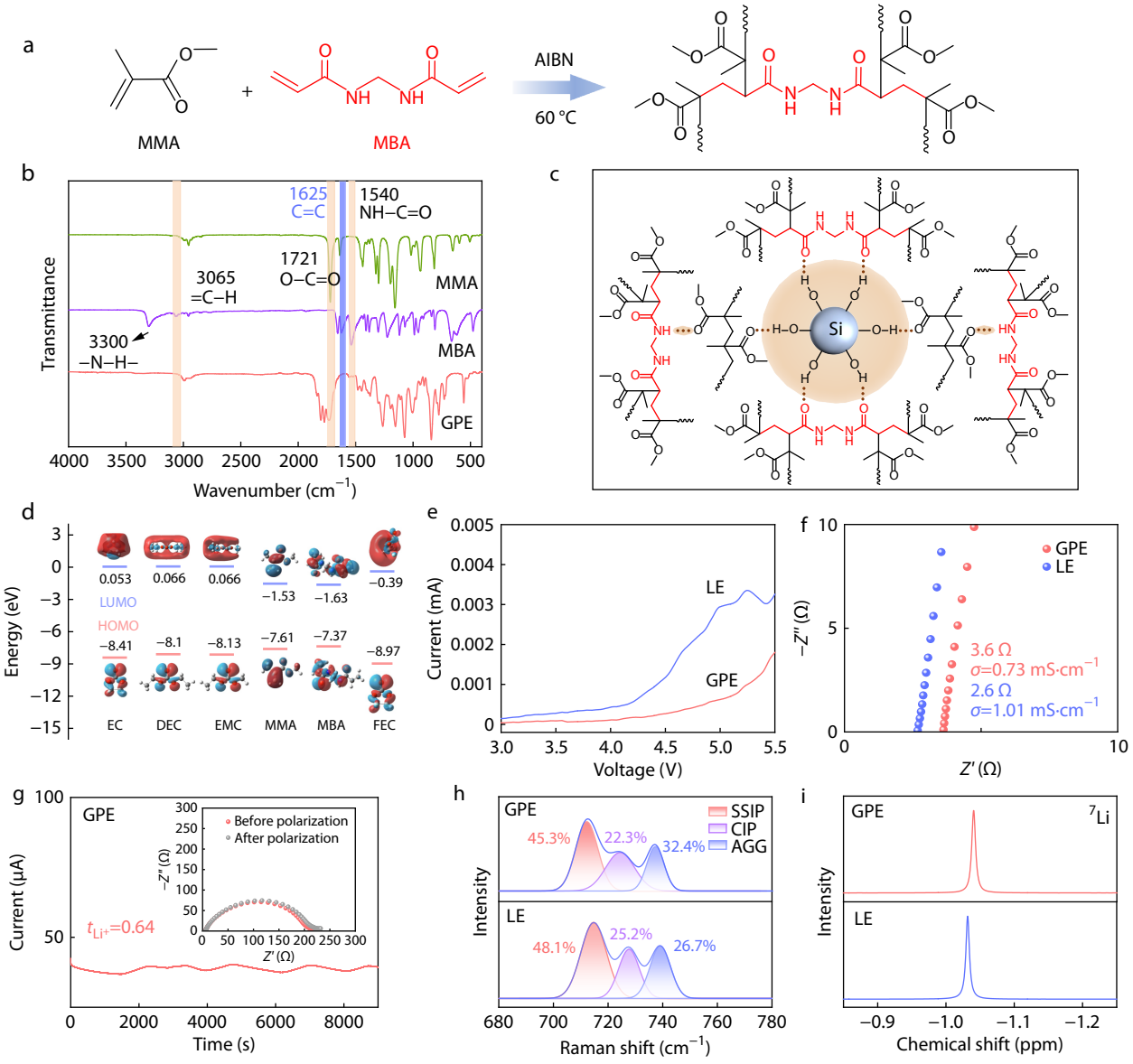

Fig. 2 Preparation and characterization of PMMA-GPE. (a) *In situ* polymerization process of MMA and MBA; (b) FTIR spectra of MMA, MBA, and PMMA-GPE; (c) Schematic illustration of the hydrogen bond between polymer chains and silicon particles; (d) HOMO and LUMO energy levels of the electrolyte components; (e) Electrochemical stability windows of different electrolytes at room temperature; (f) Ionic conductivities of different electrolytes; (g) Lithium-ion transference number of PMMA-GPE; (h) Raman spectra and (i) ^{7}Li NMR spectra of PMMA-GPE and LE.

proportions of solvent-separated ion pairs (SSIPs), contact ion pairs (CIPs), and cation-anion aggregates (AGGs) were analyzed to evaluate the coordination behavior of PF_6^- in different electrolytes. The results indicate that a larger proportion of PF_6^- participates in CIP and AGG in PMMA-GPE, which strengthens anion coordination and reduces the amount of solvent molecules within the solvation sheath. This solvation structure was further confirmed by nuclear magnetic resonance (NMR) spectroscopy (Fig. 2i). Compared with LE, the high-field shift of the ^{7}Li-NMR peak observed in PMMA-GPE suggests a higher concentration of ion clusters in the electrolyte. The unique polymer network structure of PMMA-GPE confines PF_6^- within the coordination sheath, while the C=O groups in the polymer matrix enhance the charge density around Li^+ through strong ionic interactions with lithium ions. As a result, such a solvation structure not only reduces the desolvation energy barrier of Li^+ but also promotes Li^+ transport and improves ionic conductivity.

The electrochemical performance of high-mass-loading Si anodes at 3.5 mg·cm^{-2} was evaluated in a PMMA-GPE using Li as the counter electrode. For comparison, LE was also tested under the same conditions. Fig. 3(a) shows the cycling performance of the Si anodes in different electrolytes. In PMMA-GPE, the Si anode exhibited high initial discharge and charge capacities of 1656.4 and 1462.4 mAh·g^{-1}, respectively, corresponding to a high initial coulombic efficiency (ICE) of 88.3% and good cycling stability with a high capacity retention of 81.0% after 100 cycles. In contrast, it underwent rapid capacity degradation in LE, with a low capacity retention of 52.8% after only 70 cycles. The excellent cycling performance of PM-

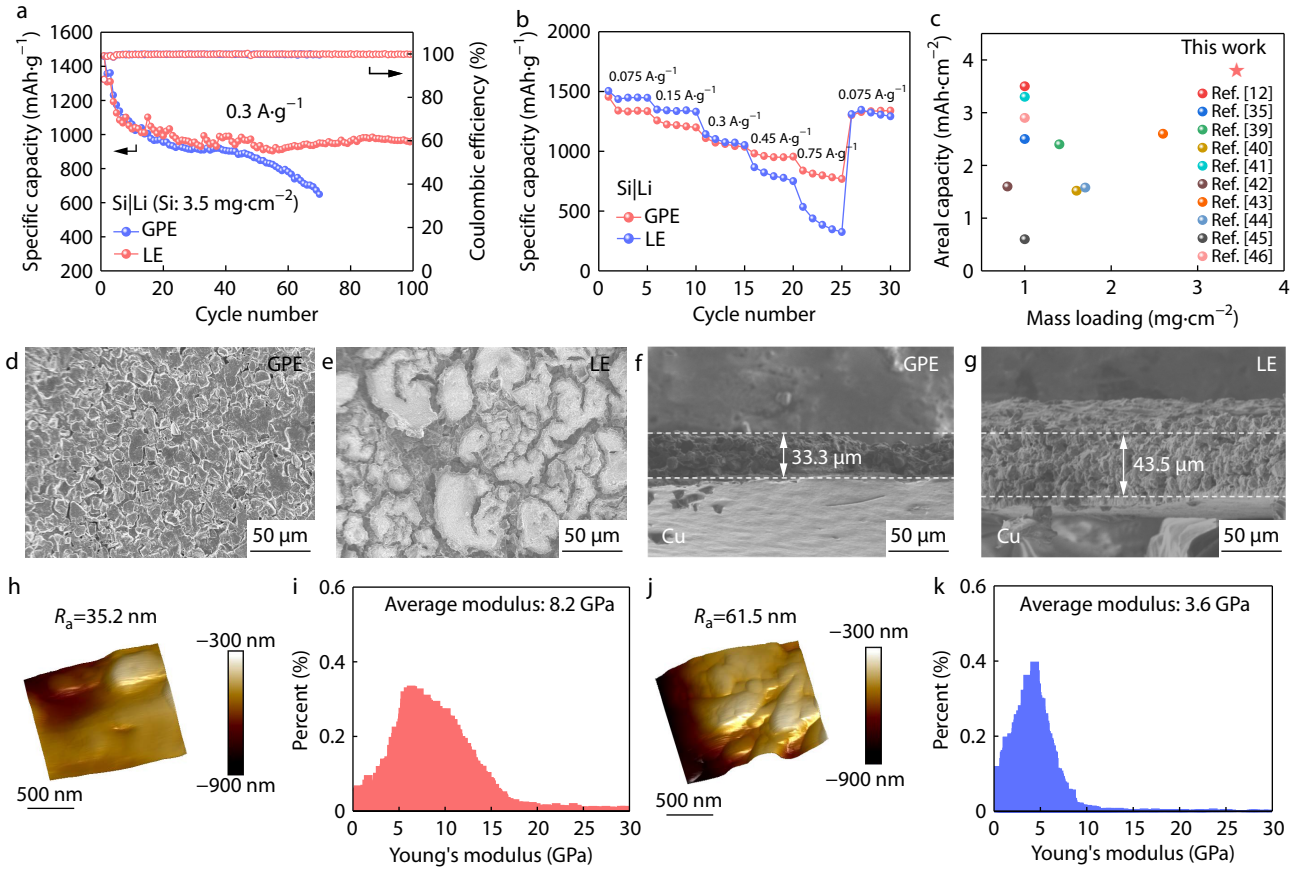

Fig. 3 Electrochemical performance and morphological characterization of the Si anodes in different electrolytes. (a) Cycling performance at 0.3 A·g^{-1}; (b) Rate capability; (c) Performance comparison of Si anodes in this work and previously reported; (d, e) Top-view and (f, g) cross-section SEM images of the Si anode after 100 cycles in (d, f) GPE and (e, g) LE. AFM images and corresponding surface roughness (R_a) of the cycled Si anodes in (h, i) GPE and (j, k) LE.

MA-GPE can be attributed to hydrogen bonding interactions, which effectively stabilize the silicon particles and enhance the cycling stability of the Si anode. To further investigate the effects of hydrogen bonding, a gel polymer electrolyte was prepared using ethylene glycol diacrylate (EGDA), which is a crosslinking agent that does not form hydrogen bonds with MMA. The GPE with the MBA crosslinker showed better performance than the GPE with the EGDA crosslinker, suggesting that sufficient hydrogen bonding interactions in the PMMA-GPE play an important role in stabilizing the silicon anode (Fig. S5 in ESI). In addition, an improved rate performance was obtained for PMMA-GPE compared to LE (Fig. 3b). The performance of the high-mass-loading Si anode in PMMA-GPE surpasses that of previous reports on Si anodes in half-cells,[12,35,39–46] highlighting the critical role of PMMA-GPE in stabilizing silicon anodes (Fig. 3c and Table S1 in ESI).

The reaction kinetics of the Si anode in the PMMA-GPE and LE were evaluated using the galvanostatic intermittent titration technique (GITT). As shown in Fig. S6 (in ESI), the lithium-ion diffusion coefficient (D_{Li^+}) in the PMMA-GPE was comparable to that in the LE during the deintercalation process, indicating that the incorporation of PMMA-GPE did not significantly hinder lithium-ion diffusion within the electrode.

The structural stability of the Si anode was examined using scanning electron microscopy (SEM) after cycling. The surface morphologies of the Si anode after 100 cycles are shown in Figs. 3(d) and 3(e). Severe cracking occurred in the LE, indicating substantial structural degradation during cycling. In contrast, the Si anode cycled in the PMMA-GPE retained a relatively uniform and intact surface morphology, closely resembling the pristine electrode (Fig. S7 in ESI). Cross-sectional SEM images further reveal that the thickness of the cycled Si electrode in LE increased from an initial 28.3 μm to 43.5 μm after cycling (Fig. S7 in ESI and Fig. 3g), corresponding to a 53.7% volume expansion. In contrast, the electrode cycled in PMMA-GPE showed only a slight increase in thickness to 33.3 μm, representing a much lower expansion of 17.7% (Fig. 3f). These results demonstrate that PMMA-GPE effectively mitigates the volume expansion of the Si electrode.

In addition to variations in electrode thickness, significant volume change and particle cracking can also lead to an increase in the surface roughness of the electrode. The surface morphologies of the cycled electrodes were further examined using atomic force microscopy (AFM). As shown in Fig. 3(j), the Si anode cycled in the LE exhibited a high average roughness (R_a) value of 61.5 nm. In contrast, the electrode cycled in PMMA-GPE displayed a significantly lower R_a value of 35.2 nm (Fig. 3h), indicating a more stable structure. In addition, the SEI formed in the PMMA-GPE showed a higher modulus than that in the LE (Figs. 3i and 3k). This high-modulus

SEI layer effectively withstood the mechanical stress induced by the volume expansion of the Si anode, further contributing to the improved structural integrity and stability of the electrode.

To evaluate the stability of the cathode electrolyte interphase (CEI), the performance of the NCM811 cathode was tested. As shown in Fig. S8 (in ESI), in the PMMA-GPE, a high capacity retention of 88.1% was retained after 140 cycles at a cut-off voltage of 4.3 V, whereas severe capacity fading occurred after only 60 cycles in the LE. To further investigate the effects of the electrolytes on the cathodes, transition metal (TM) dissolution was measured by probing the electrolytes after 100 cycles using inductively coupled plasma optical emission spectroscopy (ICP-OES). As shown in Fig. S9 (in ESI), the concentrations of Ni, Co, and Mn dissolved from the NCM811 cathode were significantly lower in the PMMA-GPE than in the LE. In particular, the dissolution of Ni was markedly suppressed, indicating that the PMMA-GPE also facilitated the formation of a stable and robust CEI layer on the cathode surface.

The chemical composition and depth distribution of the SEI formed on the Si electrode after 100 cycles were investigated using X-ray photoelectron spectroscopy (XPS) combined with Ar^+ sputtering depth profiling. The C 1s spectra show that the contents of C=O and C—O species gradually decrease with increasing sputtering depth in PMMA-GPE (Fig. 4a), indicating that organic components are mainly located in the outer SEI layer. In contrast, both the outer and inner layers of the SEI formed in the LE contain abundant organic species (Fig. 4b). The organic-rich outer SEI layer formed in the PMMA-GPE exhibits good elasticity, which can accommodate the repeated volume changes of the Si particles, thereby improving the electrode integrity. In addition, the reduced intensity of the Li_2CO_3 signal in the PMMA-GPE indicates that parasitic side reactions on the silicon anode are effectively suppressed. The F 1s spectra revealed that the SEI formed on the cycled Si electrode mainly consisted of LiF and $Li_xPO_yF_z$ species, which originated from the decomposition of $LiPF_6$ and FEC (Figs. 4c and 4d). Notably, LiF formed in the PMMA-GPE remained abundant throughout the sputtering process, indicating the formation of a LiF-rich SEI inner layer. Owing to its high mechanical strength and high Young's modulus, this LiF-rich SEI layer can effectively accommodate the volume expansion of the Si anode. Furthermore, the SEI formed in PMMA-GPE contained a lower proportion of $Li_xPO_yF_z$, suggesting that PMMA-GPE suppressed the decomposition of $LiPF_6$ on the anode surface.

The elemental distribution of the SEI in PMMA-GPE at different sputtering depths is summarized in Figs. 4(e) and 4(f). With increasing sputtering time, the carbon content associated with organic decomposition products gradually decreased, while the fluorine content increased. These results confirm the formation of an inorganic-rich SEI inner layer in the PMMA-GPE. Such an inorganic-dominated SEI possesses superior mechanical robustness and structural stability, which effectively enhances the stability of the Si anode and prolongs its cycling stability of the Si anode, with improved safety.

The practicability of the high-mass-loading Si anode with the PMMA-GPE was evaluated in Si|NCM811 full cells. For comparison, LE was also tested in Si|NCM811 full cells. As shown in Fig. 5(a), the PMMA-GPE cells showed remarkably

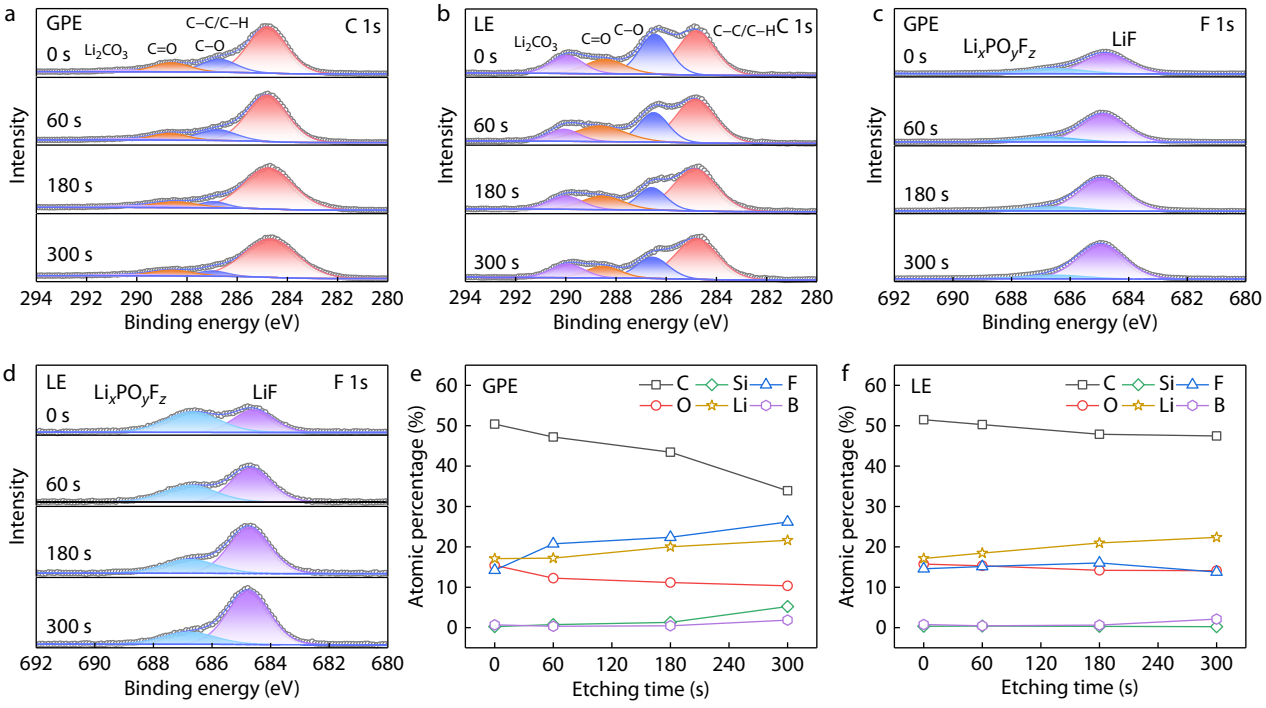

Fig. 4 Composition characterization of the SEI layers on the Si anodes after 100 cycles in different electrolytes. XPS C 1s spectra of the cycled Si anode in (a) GPE and (b) LE; XPS F 1s spectra of the cycled Si anodes in (c) GPE and (d) LE. Evolution of the atomic ratios of C, Si, F, O, Li, and B during depth profiling of the cycled Si anode in (e) GPE and (f) LE.

https://doi.org/10.1007/s10118-026-3763-x

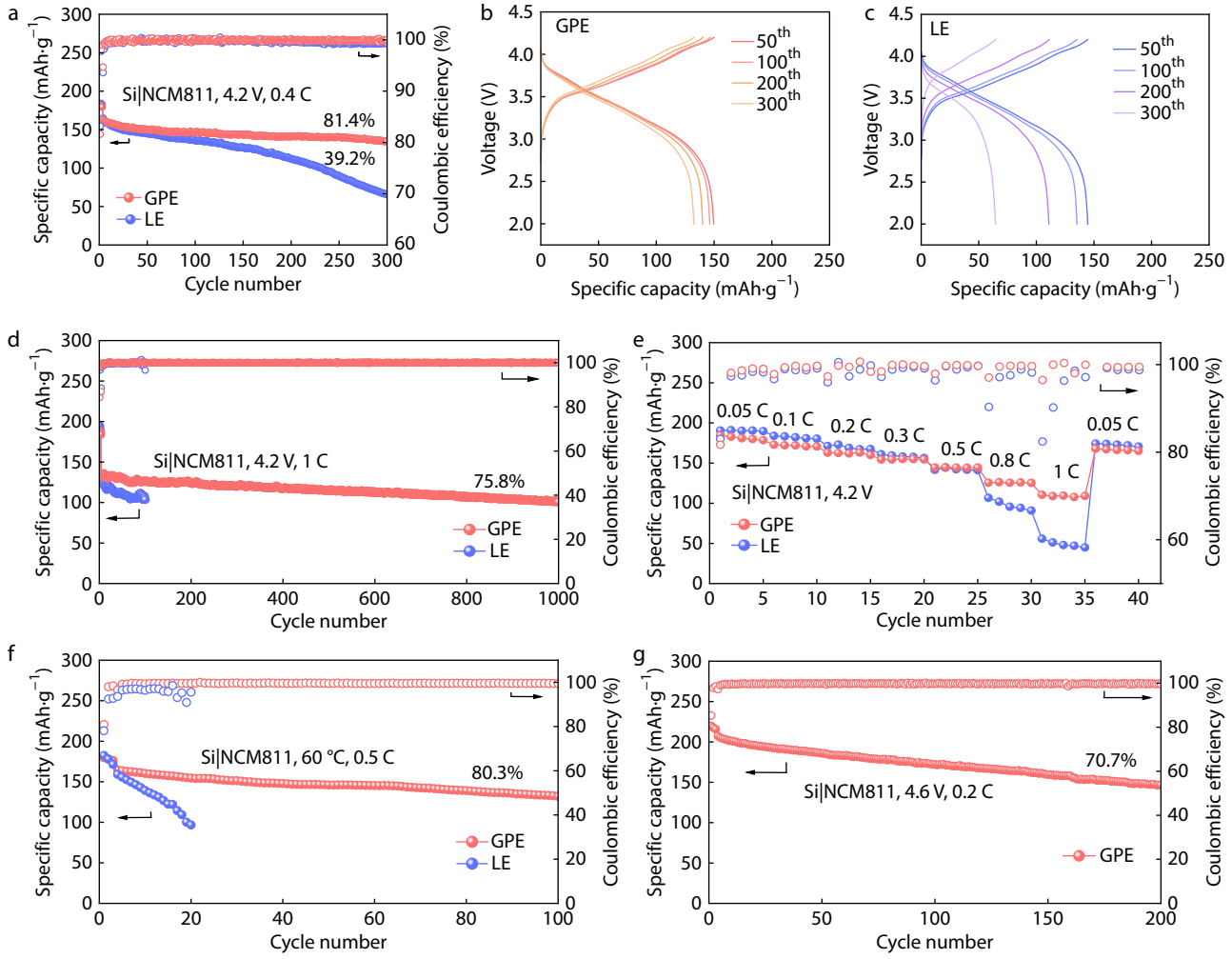

Fig. 5 Electrochemical performance of the Si|NCM811 cells with GPE and LE. (a) Cycling performance at a cut-off voltage of 4.2 V under 0.4 C; Charge-discharge profiles in different cycles with (b) GPE and (c) LE; (d) Long-term cycling performance at a cut-off voltage of 4.2 V under 1 C; (e) Rate performance of the Si|NCM811 cells with GPE and LE; (f) Cycling performance at 60 °C; (g) Cycling performance at a high cut-off voltage of 4.6 V.

improved cycling stability compared to the LE cells, with capacity retentions of 81.4% versus 39.2% after 300 cycles at 0.4 C with a cut-off voltage of 4.2 V (Figs. 5a–5c).

The long-term cycling performance was further evaluated at a higher rate of 1 C (Fig. 5d). The PMMA-GPE cells maintained 75.8% of their initial capacity after 1000 cycles, whereas the LE cells experienced significant degradation after only 100 cycles, accompanied by pronounced voltage polarization (Fig. S10 in ESI). This stability was also confirmed by electrochemical impedance spectroscopy (EIS) measurements, which showed stable impedance over 100 cycles, indicating the stable structure of the Si anode (Fig. S11 in ESI). The performance of the PMMA-GPE cells surpassed that of previously reported silicon-based full cells (Table S2 in ESI), demonstrating the great potential of PMMA-GPE for high-energy-density silicon-based lithium batteries.

The PMMA-GPE cells also exhibited an enhanced rate capability over the LE cells (Fig. 5e). At 1 C, the PMMA-GPE cells delivered a discharge specific capacity of 109.0 mAh·g^{-1}, significantly higher than 44.8 mAh·g^{-1} for the LE cells. The advantages of the PMMA-GPE cells were further validated by their excellent performance at an elevated temperature of 60 °C and a higher cutting voltage of 4.6 V. At 60 °C, the PMMA-GPE cells maintained 80.3% capacity retention after 100 cycles at 0.5 C, while the LE cells suffered rapid capacity decay after only 20 cycles due to severe interfacial side reactions (Fig. 5f). At a higher cut-off voltage (4.6 V, the PMMA-GPE cells could sustain 70.7% capacity after 200 cycles, with stable voltage polarization (Fig. 5g and Fig. S12 in ESI).

CONCLUSIONS

In summary, an *in situ* polymerized GPE was developed for high-mass-loading Si anodes. PMMA-GPE forms hydrogen bonds with the hydroxyl groups on the surface of the silicon electrode, effectively enhancing the structural integrity and surface stability of the silicon anode during cycling. It demonstrated excellent electrochemical performance on a high-mass-loading Si anode (3.5 mg·cm^{-2}), achieving a high reversible capacity of 1462.4 mAh·g^{-1}. Furthermore, with the PMMA-GPE, the full cells using the high-mass-loading Si anode and NCM811 cathode cell exhibited long-term cycling stability, with 75.8% capacity reten-

https://doi.org/10.1007/s10118-026-3763-x

tion after 1000 cycles at 1 C, even at an elevated temperature of 60 °C and a high cut-off voltage of 4.6 V. Our findings provide an effective strategy for stabilizing high-mass-loading silicon anodes using GPE, paving the way for high-energy-density LIBs.

Conflict of Interests

The authors declare no interest conflict.

Electronic Supplementary Information

Electronic supplementary information (ESI) is available free of charge in the online version of this article at http://doi.org/10.1007/s10118-026-3763-x.

Data Availability Statement

The data supporting the findings of this study are available upon reasonable request from the authors.

ACKNOWLEDGMENTS

This work was financially supported by the National Natural Science Foundation of China (No. 22579126).

REFERENCES

1 Li, Y.; Lu, Y.; Adelhelm, P.; Titirici, M.; Hu, Y. Intercalation chemistry of graphite: alkali metal ions and beyond. *Chem. Soc. Rev.* **2019**, *48*, 4655–4687.
2 Zhou, M.; Bai, P.; Ji, X.; Yang, J.; Wang, C.; Xu, Y. Electrolytes and interphases in potassium ion batteries. *Adv. Mater.* **2021**, *33*, 2003741.
3 Li, M.; Hicks, R. P.; Chen, Z.; Luo, C.; Guo, J.; Wang, C.; Xu, Y. Electrolytes in organic batteries. *Chem. Rev.* **2023**, *123*, 1712–1773.
4 He, J.; Deng, Y.; Han, J.; Xu, T.; Qi, J.; Li, J.; Zhang, Y.; Zhao, Z.; Li, Q.; Xiao, J.; Zhang, J.; Kong, D.; Wei, W.; Wu, S.; Yang, Q. Sieving pore

Graphical Abstract

Hydrogen Bonding in Gel Polymer Electrolyte Enables High Performance High-mass-loading Silicon Anode

Xin-Ran Bi, Ze-Hui Fan, Lan-Hua Ma, and Yun-Hua Xu

Tianjin University

The crosslinked gel polymer electrolyte forms hydrogen bonds with the silicon anode, effectively stabilizing high-mass-loading silicon electrodes for high-energy-density Li-ion batteries.

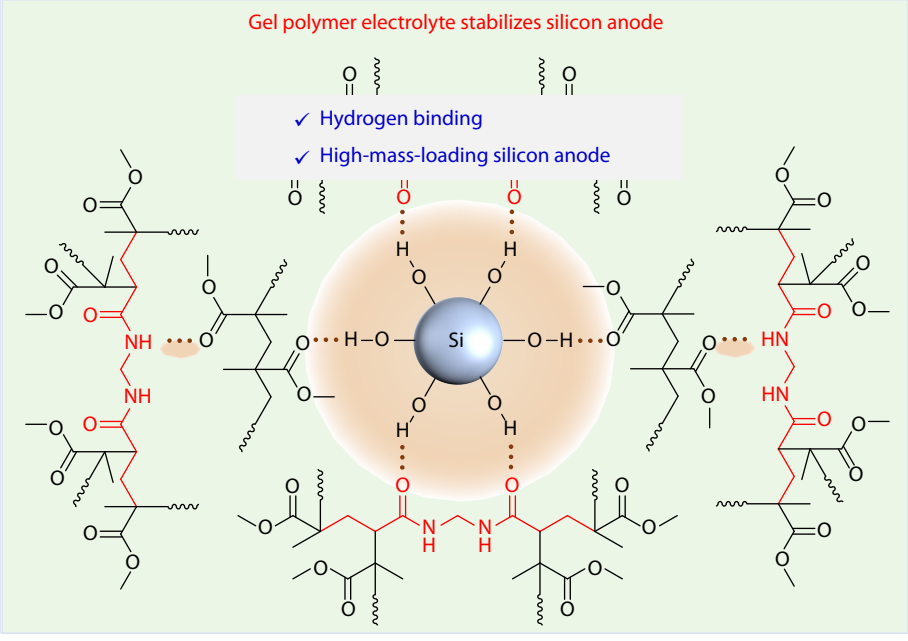

design enables stable and fast alloying chemistry of silicon negative electrodes in Li-ion batteries. *Nat. Commun.* **2025**, *16*, 4858.
5 Qi, J.; Li, Z.; Xu, T.; Yue, X.; Yin, X.; Xin, X.; Wu, S.; Liu, C.; Yang, Q. Local electrochemical co-sintering enables stable high-loading all-solid-state silicon anodes in Li-ion batteries. *Adv. Energy Mater.* **2026**, *16*, e04822.
6 Xu, Y.; Zhu, Y.; Liu, Y.; Wang, C. Electrochemical performance of porous carbon/Tin composite anodes for sodium-ion and lithium-ion batteries. *Adv. Energy Mater.* **2013**, *3*, 128−133.
7 Xu, Y.; Zhu, Y.; Wang, C. Mesoporous carbon/silicon composite anodes with enhanced performance for lithium-ion batteries. *J. Mater. Chem. A* **2014**, *2*, 9751−9757.
8 Cai, C.; Fan, Z.; Xu, Y. $Li_{1.3}Al_{0.3}Ti_{1.7}(PO_4)_3$-coated ternary cathode materials for high performance lithium-ion batteries. *Chem. Res. Chin. Univ.* **2025**, *41*, 1620−1627.
9 Li, M.; Yang, J.; Shi, Y.; Chen, Z.; Bai, P.; Su, H.; Xiong, P.; Cheng, M.; Zhao, J.; Xu, Y. Soluble organic cathodes enable long cycle life, high rate, and wide-temperature lithium-ion batteries. *Adv. Mater.* **2022**, *34*, 2107226.
10 Wang, W.; Zhao, C.; Yang, J.; Xiong, P.; Su, H.; Xu, Y. In-situ electropolymerized bipolar organic cathode for stable and high-rate lithium-ion batteries. *Sci. China Mater.* **2021**, *64*, 2938−2948.
11 Li, R.; Zeng, J.; Wang, P.; He, T.; Rao, L.; Zhou, L.; Hou, M.; Zhang, X.; Lin, T.; Zhang, Y.; Zhang, N. A high-performance silicon-based anode enabled by hybrid pathways for all-solid-state batteries. *Adv. Energy Mater.* **2025**, *15*, e02913.
12 Bai, M.; Tang, X.; Zhang, M.; Wang, H.; Wang, Z.; Shao, A.; Ma, Y. An in-situ polymerization strategy for gel polymer electrolyte Si||Ni-rich lithium-ion batteries. *Nat. Commun.* **2024**, *15*, 5375.
13 Chan, C. K.; Peng, H.; Liu, G.; McIlwrath, K.; Zhang, X. F.; Huggins, R. A.; Cui, Y. High-performance lithium battery anodes using silicon nanowires. *Nat. Nanotechnol.* **2008**, *3*, 31−35.
14 Zhang, Y.; Zhang, Y.; Wang, X.; Gong, H.; Cao, Y.; Ma, K.; Zhang, S.; Wang, S.; Yang, W.; Wang, L.; Sun, J. Trace multifunctional additive enhancing 4.8 V ultra-high voltage performance of Ni-rich cathode and SiO_x anode battery. *Adv. Energy Mater.* **2025**, *15*, 2403751.
15 Yu, R.; Pan, Y.; Jiang, Y.; Zhou, L.; Zhao, D.; Van Tendeloo, G.; Wu, J.; Mai, L. Regulating lithium transfer pathway to avoid capacity fading of nano Si through sub-nano scale interfused SiO_x/C coating. *Adv. Mater.* **2023**, *35*, 2306504.
16 An, W.; Gao, B.; Mei, S.; Xiang, B.; Fu, J.; Wang, L.; Zhang, Q.; Chu, P. K.; Huo, K. Scalable synthesis of ant-nest-like bulk porous silicon for high-performance lithium-ion battery anodes. *Nat. Commun.* **2019**, *10*, 1447.
17 Liu, Z.; Zhang, Y.; Wang, S.; Xiong, J.; Gao, T.; Yu, R.; Xu, Z.; Chen, X.; Li, J.; Lin, Z.; Zheng, M.; Xia, Y.; He, P. Solvation-shell engineering enables additive-dominated coordination for stable silicon anodes under minimal salt conditions. *Angew. Chem. Int. Ed.* **2026**, *65*, e18092.
18 Xia, M.; Zhang, H.; Lin, Y.; Xu, C.; Gu, J.; Pan, S.; Zhang, H.; Gong, Z.; Yang, Y. The alternating stress evolution and buffering effects in all-solid-state lithium-sulfur battery with pre-lithiated silicon-based anode. *Adv. Funct. Mater.* **2026**, *36*, e13271.
19 Liang, B.; Liu, Y.; Xu, Y. Silicon-based materials as high capacity anodes for next generation lithium ion batteries. *J. Power Sources* **2014**, *267*, 469−490.
20 Zhai, Y.; Zhong, Z.; Kuang, N.; Li, Q.; Xu, T.; He, J.; Li, H.; Yin, X.; Jia, Y.; He, Q.; Wu, S.; Yang, Q. Both resilience and adhesivity define solid electrolyte interphases for a high performance anode. *J. Am. Chem. Soc.* **2024**, *146*, 15209−15218.
21 Pan, S.; Han, J.; Wang, Y.; Li, Z.; Chen, F.; Guo, Y.; Han, Z.; Xiao, K.; Yu, Z.; Yu, M.; Wu, S.; Wang, D.; Yang, Q. Integrating SEI into layered conductive polymer coatings for ultrastable silicon anodes. *Adv. Mater.* **2022**, *34*, 2203617.
22 Lu, Z.; Zhao, Y.; Xu, D.; Hua, Z.; Chen, J.; He, X.; Zhang, X.; Zhang, J.; Shi, J.; Wen, R.; Li, G.; Guo, Y.; Wan, L. Constructing functional lithium-ion transport interfaces by in-situ growth and transformation on chemical vapor deposition-derived silicon-carbon anode materials. *J. Am. Chem. Soc.* **2026**, *148*, 9103−9113.
23 Su, H.; Zhang, H.; Chen, Z.; Li, M.; Zhao, J.; Xun, H.; Sun, J.; Xu, Y. Electrolyte and interphase engineering through solvation structure regulation for stable lithium metal batteries. *Chin. Chem. Lett.* **2023**, *34*, 108640.
24 Liu, N.; Lu, Z.; Zhao, J.; McDowell, M. T.; Lee, H.; Zhao, W.; Cui, Y. A pomegranate-inspired nanoscale design for large-volume-change lithium battery anodes. *Nat. Nanotechnol.* **2014**, *9*, 187−192.
25 Xin, X.; Yin, Q.; Zhao, Z.; Qi, J.; Xu, T.; Li, Z.; Li, F.; Chen, F.; Wu, S.; Yang, Q. Wheel-hub-inspired silicon anodes with superior stress tolerance for high-energy lithium-ion batteries. *Adv. Energy Mater.* **2026**, *16*, e06650.
26 Magasinski, A.; Dixon, P.; Hertzberg, B.; Kvit, A.; Ayala, J.; Yushin, G. High-performance lithium-ion anodes using a hierarchical bottom-up approach. *Nat. Mater.* **2010**, *9*, 353−358.
27 Chen, G.; Xie, H.; Luo, J.; Tao, S.; Bao, W.; Qu, Y.; Gao, S.; Tian, S.; Xu, X.; Han, S.; Cao, Z.; Chen, Y.; Xiong, S.; Wan, J. High-density sub-10 nm silicon nanowires fabricated *via* directed self-assembly and sequential infiltration synthesis synergistic patterning for multiple applications. *ACS Nano* **2026**, *20*, 7483−7495.
28 Choi, S.; Kwon, T.; Coskun, A.; Choi, J. W. Highly elastic binders integrating polyrotaxanes for silicon microparticle anodes in lithium ion batteries. *Science* **2017**, *357*, 279−283.
29 Li, A.; Wang, Z.; Lee, T.; Zhang, N.; Li, T.; Zhang, W.; Jayawardana, C.; Yeddala, M.; Lucht, B. L.; Wang, C. Asymmetric electrolyte design for high-energy lithium-ion batteries with micro-sized alloying anodes. *Nat. Energy* **2024**, *9*, 1551−1560.
30 Fan, Z.; Liu, Y.; Su, H.; Chi, S.; Dong, Q.; Liu, Y.; Wang, L.; Yang, Q.; Xu, Y. Surface reaction regulation for high-voltage and safe quasi-solid-state lithium metal batteries. *Chem. Eng. J.* **2026**, *527*, 171745.
31 Zhao, J.; Li, M.; Su, H.; Liu, Y.; Bai, P.; Liu, H.; Ma, L.; Li, W.; Sun, J.; Xu, Y. In situ fabricated non-flammable quasi-solid electrolytes for Li-metal batteries. *Small Meth.* **2023**, *7*, 2300228.
32 Xia, W.; Zhang, Y.; Zheng, R.; Chen, R.; Yan, Y.; Wu, N.; Xin, S. Building a safe and stable rechargeable lithium-metal battery by applying a flame-retardant, double-network structural hybrid polyester-based quasi-solid-state polymer electrolyte. *Sci. China Mater.* **2025**, *68*, 2567−2572.
33 Li, X.; Qian, K.; He, Y.; Liu, C.; An, D.; Li, Y.; Zhou, D.; Lin, Z.; Li, B.; Yang, Q.; Kang, F. A dual-functional gel-polymer electrolyte for lithium ion batteries with superior rate and safety performances. *J. Mater. Chem. A* **2017**, *5*, 18888−18895.
34 Zhao, E.; Luo, S.; Gu, Y.; Yang, L.; Hirano, S. Preactivation strategy for a wide temperature range *in situ* gel electrolyte-based $LiNi_{0.5}Co_{0.2}Mn_{0.3}O_2$ // Si-graphite battery. *ACS Appl. Mater. Interfaces* **2021**, *13*, 59843−59854.
35 Liu, Q.; Feng, Y.; Liu, J.; Liu, Y.; Cui, X.; He, Y.; Nuli, Y.; Wang, J.; Yang, J. In situ integration of a flame retardant quasisolid gel polymer electrolyte with a Si-based anode for high-energy Li-ion batteries. *ACS Nano* **2024**, *18*, 13384−13396.
36 Huang, Q.; Song, J.; Gao, Y.; Wang, D.; Liu, S.; Peng, S.; Usher, C.; Goliaszewski, A.; Wang, D. Supremely elastic gel polymer electrolyte enables a reliable electrode structure for silicon-based anodes. *Nat. Commun.* **2019**, *10*, 5586.
37 Li, L.; Wang, M.; Wang, J.; Ye, F.; Wang, S.; Xu, Y.; Liu, J.; Xu, G.; Zhang, Y.; Zhang, Y.; Yan, C.; Medhekar, N. V.; Liu, M.; Zhang, Y. Asymmetric gel polymer electrolyte with high lithium ion conductivity for dendrite-free lithium metal batteries. *J. Mater.*

Chem. A **2020**, *8*, 8033–8040.
38 Bai, M.; Yang, L.; Jia, Q.; Tang, X.; Liu, Y.; Wang, H.; Zhang, M.; Guo, R.; Ma, Y. Encasing prelithiated silicon species in the graphite scaffold: An enabling anode design for the highly reversible, energy-dense cell model. *ACS Appl. Mater. Interfaces* **2020**, *12*, 47490–47502.
39 Liu, F.; Zeng, Y.; Li, Z.; Liu, Y.; Chen, X.; Jiang, Y.; Shao, H.; Guo, J.; Xu, X.; Pan, F.; Deng, Y.; Wang, J.; Shao, M. A gel polymer electrolyte with multiple hydrogen bonding for pressure-free Ah silicon-based pouch cells. *Nat. Commun.* **2025**, *16*, 11708.
40 Ma, Z.; Ruan, D.; Wang, D.; Lu, Z.; He, Z.; Guo, J.; Fan, J.; Jiang, J.; Wang, Z.; Luo, X.; Ma, J.; Zhang, Z.; You, Y.; Jiao, S.; Cao, R.; Ren, X. Selective methylation of cyclic ether towards highly elastic solid electrolyte interphase for silicon-based anodes. *Angew. Chem. Int. Ed.* **2025**, *64*, e202414859.
41 Cho, Y.; Park, H.; Lee, J.; Hwang, C.; Jeon, Y.; Park, S.; Song, H. Organogel electrolyte for high-loading silicon batteries. *J. Mater. Chem. A* **2016**, *4*, 8005–8009.
42 Cheng, Z.; Chen, W.; Zhang, Y.; Xiang, J.; Tang, D.; Ji, H.; Li, J.; Huang, Y.; Yuan, L. Enhanced cycleability of micron-size silicon anode by in situ polymerized polymer electrolyte. *Adv. Funct. Mater.* **2024**, *34*, 2408145.
43 Chae, S.; Kwak, W.; Han, K. S.; Li, S.; Engelhard, M. H.; Hu, J.; Wang, C.; Li, X.; Zhang, J. Rational design of electrolytes for long-term cycling of Si anodes over a wide temperature range. *ACS Energy Lett.* **2021**, *6*, 387–394.
44 Liu, G.; Xia, M.; Gao, J.; Cheng, Y.; Wang, M.; Hong, W.; Yang, Y.; Zheng, J. Dual-salt localized high-concentration electrolyte for long cycle life silicon-based lithium-ion batteries. *ACS Appl. Mater. Interfaces* **2023**, *15*, 3586–3598.
45 Wen, Z.; Wu, F.; Li, L.; Chen, N.; Luo, G.; Du, J.; Zhao, L.; Ma, Y.; Li, Y.; Chen, R. Electrolyte design enabling stable solid electrolyte interface for high-performance silicon/carbon anodes. *ACS Appl. Mater. Interfaces* **2022**, *14*, 38807–38814.
46 Li, Y.; Zhao, D.; Zhao, M.; Lu, P.; Luo, J.; Peng, K. Stable LiF-rich solid electrolyte interphase *via* self-polymerizing gel electrolytes boosts silicon anode cycling. *Mater. Today Energy* **2026**, *56*, 102191.

https://doi.org/10.1007/s10118-026-3763-x